Journal of Membrane Science 712 (2024) 123247

Contents lists available at ScienceDirect

Journal of Membrane Science

journal homepage: www.elsevier.com/locate/memsci

Covalent organic framework membranes achieving Mg/Li separation by permeating Mg^{2+} while retaining Li^{+}

Ming Liu [a], Mingjie Wei [a,*], Gan Liu [a], Daiwen Li [a], Zhe Zhang [b], Yong Wang [a,c]

[a] State Key Laboratory of Materials-Oriented Chemical Engineering, College of Chemical Engineering, Nanjing Tech University, Nanjing, 211816, Jiangsu, China
[b] School of Environmental Science and Engineering, Nanjing Tech University, Nanjing, 211816, Jiangsu, China
[c] School of Energy and Environment, Southeast University, Nanjing, 210096, Jiangsu, China

ARTICLE INFO

Keywords:
Covalent organic framework (COF)
Desalination
Ion rejection
Hydrophilicity
Non-equilibrium molecular dynamics simulation

ABSTRACT

Due to the growing demand for lithium in the new energy industry, significant attention has been focused on developing lithium extraction technologies from salt-lake brine. However, the high Mg/Li ratio in salt-lake brine presents challenges for membrane separation technology. If a membrane can allow Mg^{2+} and water molecules to pass through while retaining Li^{+}, the retained brine will have concentrated Li^{+} with a reduced Mg/Li ratio, creating the facilitation of further lithium extraction. In this study, we discovered through non-equilibrium molecular dynamics simulations that strongly hydrophilic covalent organic frameworks membranes capture Li^{+} in their pores, preventing additional Li^{+} from entering the nanopores. Meanwhile, Mg^{2+} can freely penetrate these nanopores along with water molecules. This adsorption of Li^{+} and the free permeation of Mg^{2+} with water molecules result in the effective separation of Li^{+} and Mg^{2+}. Consequently, the retained brine becomes lithium-rich with reduced Mg/Li ratio. The findings of this work provide valuable guidance for designing nanofiltration membranes for extracting lithium from salt lakes with high Mg/Li ratio.

1. Introduction

In recent years, the demand for lithium resources as a key raw material has surged dramatically [1–3]. Therefore, efficient separation of magnesium and lithium is particularly important for the development of lithium resources since they are widely present on the earth and often coexist in various minerals and salt lakes [4,5]. As magnesium and lithium have similar chemical properties, traditional lithium extraction methods, such as evaporative crystallization [6] and chemical precipitation [7], are often inefficient, costly, and highly time intensive [8,9]. Therefore, exploring efficient, low-cost, and environmentally friendly magnesium-lithium separation technologies has become an important research direction in the field of lithium extraction.

A crucial step among the technology of salt lake lithium extraction industry involves adding precipitants such as sodium carbonate and calcium hydroxide to the brine to remove impurities like magnesium and calcium, and then producing lithium carbonate from the refined brine [10]. Mg^{2+} can be removed due to the differing solubilities of carbonates of lithium and magnesium. Lithium carbonate, as one of the most important products in the lithium industry, serves as a critical raw material for producing other downstream lithium products [11]. However, for brines with high magnesium-to-lithium (Mg/Li) ratio, removing Mg^{2+} requires a substantial amount of precipitant, which significantly increases industrial production costs [12]. To reduce Mg/Li ratio before using the precipitation method, membrane separation technology has been introduced into brine treatment [13,14]. It can selectively retain Mg^{2+} while allowing Li^{+} to pass through due to the pore size sieving and Donnan effect of the nanofiltration membranes [15]. However, water molecules pass through the membrane more readily than either of these two ions, which often results in a reduced concentration of Li^{+}. A subsequent reverse osmosis process is needed to concentrate the brine further since efficient production of lithium carbonate requires the concentration of Li^{+} in the refined brine to reach at least 10 g/L [11]. If there exists one kind of membrane which can preferentially permeate Mg^{2+} and water molecules while retaining Li^{+}, it could achieve reduced Mg/Li ratio while simultaneously increasing the concentration of Li^{+} in the concentrated brine.

Covalent organic frameworks (COFs) have shown great potential in the field of separation science in recent years due to their unique structure and properties [16,17]. COFs are a class of materials made up of covalently bonded organic molecular frameworks, featuring highly ordered porous structures, uniform pore size, high surface areas, and

* Corresponding author.
E-mail address: mj.wei@njtech.edu.cn (M. Wei).

https://doi.org/10.1016/j.memsci.2024.123247
Received 2 July 2024; Received in revised form 20 August 2024; Accepted 21 August 2024
Available online 26 August 2024

good chemical stability [18]. These characteristics make COFs widely promising in applications such as gas storage, separation, catalysis, and energy storage [19]. High selectivity in the adsorption or filtration of specific metal ions can be achieved through finely tuning the pore size and functionalizing the surface groups of COFs [20,21]. It offers a new solution for enhancing the efficiency and reducing the costs of lithium extraction from salt lakes. Since the hydrated diameters of Li^+ (7.64 Å) is slightly smaller than that of Mg^{2+} (8.56 Å) and the hydration shell of Li^+ is softer, the Li^+ is preferable to penetrate the COFs with pore size of ~8 Å while Mg^{2+} will be retained. Consequently, most research on Mg/Li separation request COFs of small pore size, employing size sieving to exclude specific Mg^{2+}. However, researchers often overlook the impact of ion-COF interactions on separation efficiency during ion transport within the COFs. It is expected to design a kind of COFs that can preferentially permeate Mg^{2+} and water molecules because of their larger pore sizes and retain Li^+ due to their pore wall chemistry.

While the rich designability of COFs opens up many possibilities, it also presents significant challenges in screening COF materials. Identifying one kind of COFs that can achieve specific ion permeation goals from tens of thousands of possibilities is extremely difficult for experimental works. Analyzing the structure and chemical features of COFs and understanding the permeation mechanisms of different ions through these frameworks can facilitate the selection of COFs tailored to specific separation tasks. Non-equilibrium molecular dynamics (NEMD) simulations as an important complement to experimental and theoretical approaches offer unique advantages in exploring the mechanisms of ion transport through membrane pores. For instance, Wang et al. [22] utilized the NEMD method to study the separation efficiency of carbon nanotube (CNT) membranes functionalized with different groups in a mixed solution of $MgCl_2$/LiCl. They found that CNT membranes coated with carboxyl groups exhibited a stronger attraction to Mg^{2+} relative to Li^+, thereby enhancing the permeability of Mg^{2+} over Li^+. Furthermore, Zhang et al. [23] examined the detailed structure and dynamics of ion and water molecule transport in the channels of 3D–OH–COF membranes. Their findings indicated that the high-density rectangular channels in 3D–OH–COF membranes contributed to its high permeability for water and the presence of charged hydrogen atoms on the channels led to the exclusion of Na^+ and the adsorption of Cl^-.

NEMD is proven to be a powerful tool for understanding the transport behaviors of Mg^{2+} and Li^+ in the pores of COFs. In this work, we use NEMD simulations to investigate the transport behaviors of Li^+ and Mg^{2+} through COF membranes with varying hydrophilicity and hydrophobicity. The simulation results reveal that highly hydrophilic COF membranes can trap Li^+ within their pores, where the tightly adsorbed Li^+ prevents the further entry of additional Li^+ into the nanopores. Meanwhile, Mg^{2+} can freely permeate through the COF pores along with water molecules. This process selectively permeates Mg^{2+} and water molecules while intercepting Li^+, thereby achieving the goals of reducing the Mg/Li ratio and enhancing the concentration of Li^+ in brine. The findings of this work have implications for the design of nanofiltration membranes intended for lithium extraction from salt lakes with high Mg/Li ratio.

2. Simulation details

We chose TpPa with a theoretical pore size of as large as ~15.8 Å because this size was much larger than the hydrated diameters of Li^+ (7.64 Å) and Mg^{2+} (8.56 Å). Such pore size would result in the free permeation of Li^+ and Mg^{2+} if only pore size sieving effect was considered. The atomic configuration of TpPa was obtained from the CoRE COF database [24]. The *p*-phenylenediamine (Pa) in the TpPa synthesis monomer is easily grafted and modified, facilitating the adjustment of the hydrophilicity and hydrophobicity of the COF. Firstly, optimization calculations using density functional theory (DFT) were conducted using the Cambridge Sequential Total Energy theory (CASTEP). The TpPa unit cell was optimized using the generalized gradient approximation (GGA) exchange-correlation functional defined by Perdew, Burke, and Ernzerhof (PBE). The atomic charges of TpPa were calculated using the restrained electrostatic potential (RESP) method, at a computational level based on DFT with B3LYP/6-311G**. DFT calculations were performed using Gaussian09 software, considering water solvent effects with the solvation model based on density (SMD) method. RESP charge fitting utilized Multiwfn software [25]. All the NEMD simulations were carried out using the Large-scale Atomic/Molecular Massively Parallel Simulator (LAMMPS) package [26]. Interatomic interactions included 12-6 Lennard-Jones and Coulombic potentials. The LJ parameters for TpPa atoms were taken from the Dreiding force field, which has been extensively applied in simulations related to COFs [27–30]. The cut-off distances for LJ and Coulomb interactions were set to 1.0 and 1.2 nm, respectively. Long-range electrostatic interactions were calculated using the particle−particle particle-mesh (PPPM) algorithm with an accuracy of 10^{-4}. Water molecules were modeled using the SPC/E model [31] and the SHAKE algorithm was used to constrain bonds and angles. Ion parameters were referenced from literature appropriate for the SPC/E water model [32,33]. Periodic boundary conditions were applied in the *x*, *y*, and *z* directions, with the feed side and permeation side interconnected.

The built model for NEMD simulations is shown in Fig. 1. The membranes were modeled by 10 layers of TpPa. The feed side consists of a mixed solution of LiCl and $MgCl_2$, with ion concentration of 1 M, and the permeate side contains pure water. The actual Mg^{2+}/Li^+ ratio in China's Salt Lake is up to 95. However, in our simulations, higher ratio will cause very few numbers of Li^+ due to the length limitation of MD simulations. The few numbers of Li^+ will then dramatically reduce the signal-noise-ratio for Li^+. If higher Mg^{2+}/Li^+ ratio is applied, the numbers of Li^+ will be extremely low, and the mechanism of Li^+ transport through membrane will be hardly observed. In addition, since the permeate component is Mg^{2+}, the lower Mg^{2+}/Li^+ ratio will not prevent the observation of Mg^{2+} transport through membranes as there are enough Mg^{2+} in our simulations. We believe if Mg^{2+}/Li^+ ratio is applied, the selectivity of Mg/Li will be further promoted as the concentration of Li^+ adsorbed inside membranes is much higher than that in feed side, which will prevent additional Li^+ entering membranes more efficiently.

Each simulation began with a process of energy minimization con-

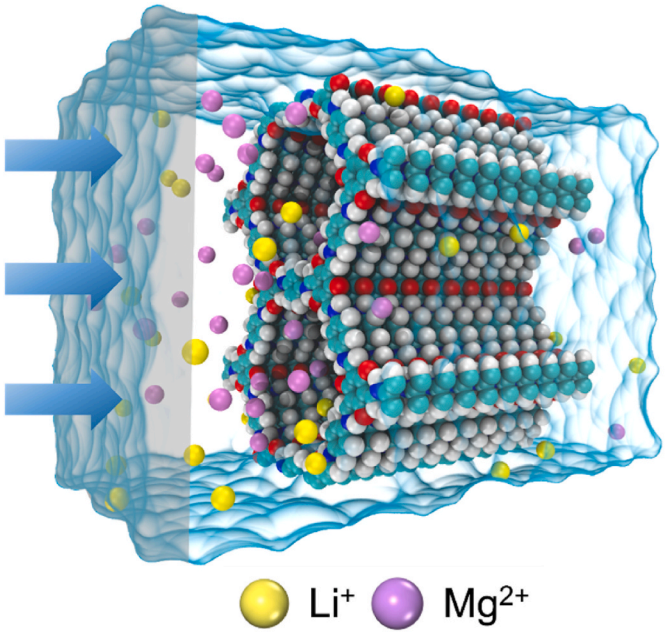

Fig. 1. Simulation model for studying the mixed salt solution transport through the TpPa membrane using the "pump" method.

ducted with a precision of 10^{-5}. Subsequently, the system temperature was controlled at 300 K using Nose-Hoover thermostat. The "pump" method was used to apply force to all atoms within a 10 Å width on the feed side, causing the membrane to withstand a ΔP of 100 MPa. The salt solution was drove through the membrane in the z-direction. The formula for ΔP calculation is described as

$$\Delta P = \frac{n_{ion} f_{ion} + n_{water} f_{water}}{A} \tag{1}$$

where ΔP is the required pressure difference, n is the number of ions or water molecules in the selected region, f is the force applied to the selected area, and A is the cross-sectional area of the membrane. This calculation method has also been introduced in our previous works [29,34,35]. The ΔP values used in the simulations are much higher than those in actual systems, the purpose of which is to enhance the signal-to-noise ratio and improve computational efficiency. This practice is also widely used in simulation studies [36,37].

Each simulation contained a pre-equilibration process first to ensure the adsorption equilibrium of ions within the membrane. Each NEMD simulation ran for at least 30–50 ns with a time step of 1 fs. The results were visualized using the VMD [38] and the simulation trajectories are saved every 1 ps. The obtained simulation trajectories were analyzed by self-compiled code. Ion rejection (R) is defined as

$$R = 1 - \frac{F_i}{n_i} \Big/ \frac{F_w}{n_w} \tag{2}$$

where F_i and F_w represent the number of ions and water molecules passing through the membrane during the simulation, respectively, n_i and n_w represent the total number of ions and water molecules in the simulation system, respectively. The formula for the selectivity of Mg/Li is as follows:

$$S_{Mg/Li} = \frac{1 - R_{Mg}}{1 - R_{Li}} \tag{3}$$

where R_{Mg} and R_{Li} represent the retention rate of Mg^{2+} and Li^{+}, respectively.

3. Results and discussion

3.1. Hydrophilicity adjustment based on partial charge

Our previous works indicates that changes in hydrophobicity and hydrophilicity significantly affect the microstate of ions within the membrane [37]. Additionally, adjustments to the atom partial charges on the pore walls can indeed alter the hydrophobicity and hydrophilicity [39,40]. Therefore, we adjust the hydrophilicity of membranes by multiplying the atom charges of TpPa with various coefficients. By this method, the influence of hydrophilicity can be exclusively investigated as the pore size of TpPa is maintained. In order to evaluate the strength of membrane hydrophilicity in molecular dynamics (MD) simulations, the self-diffusion coefficient of water molecules within the membranes is usually applied [34]. We thereby perform equilibrium MD simulations to examine the self-diffusion coefficients of pure water molecules in COFs with various adjusted charges. Since the movement of water molecules is restricted in the x and y directions due to the formation of one-dimensional pore structures in the TpPa membranes, the mean square displacement of water molecules along only the z-direction (MSD_z) is calculated within the TpPa membranes. After that, the self-diffusion coefficient (D_z) is calculated using the following formula,

$$D_z = \frac{\lim MSD_z(t)}{2t} \tag{4}$$

Results of MSD_z under diverse charge conditions are shown in Fig. 2a. The MSD_z curves are approximately linear, and the slope of each curve represents its respective D_z. The D_z values for each system under different charge conditions are calculated by Eq. (4), and the results are displayed in Fig. 2b. It is noticeable that the D_z values decrease as the atom partial charges of membranes gradually increase, indicating the enhanced hydrophilicity of the membranes.

As indicated by the work of Xu et al. [41], membrane permeability generally decreases while the membrane hydrophilicity is promoted. Therefore, the water flux of the membranes with various hydrophilicities is calculated and presented in Fig. 2c. To confirm that NEMD simulations has reach the steady state, we plot the dependence of

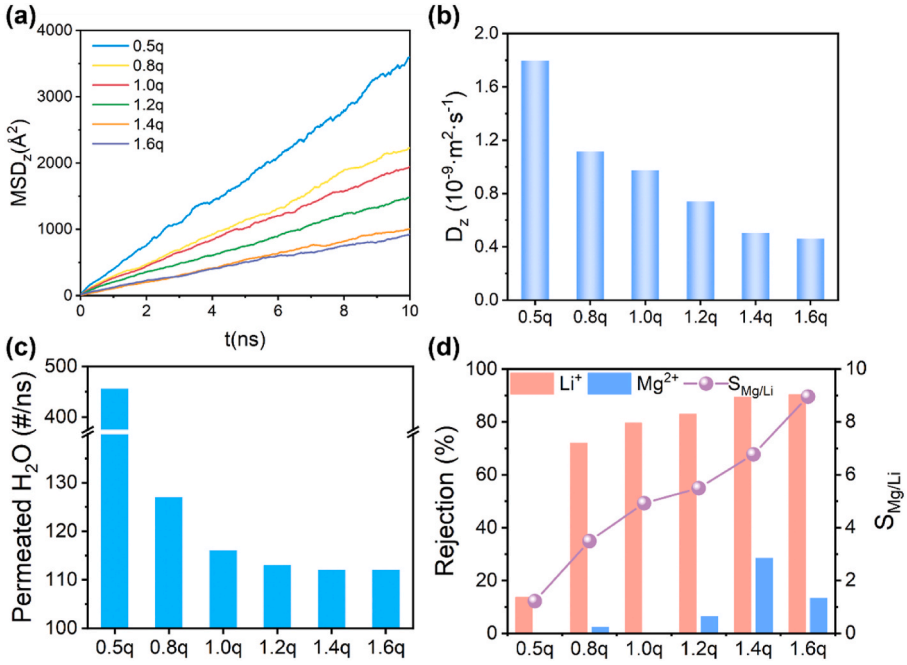

Fig. 2. (a) Mean square displacement and (b) self-diffusion coefficient of water molecules along the z-direction inside membranes of various hydrophilicity. (c) Number of water molecules passing through TpPa membranes of various hydrophilicity per unit time (ns). (d) Relationship between the retention rate of Li^{+} and Mg^{2+} and $S_{Mg/Li}$.

permeance of water molecules and ions at case of 0.5q and 1.6q in Fig. S2. The curve results show the steady state of the flow. It is evident that the water flux gradually decreases as the atom partial charges are enhanced. In the case of 0.5q, the water flux is significantly higher than that in other cases. The water flux drops sharply as the atom partial charges increase from 0.5q to 0.8q and then the decrease tendency slows down. The comparison of hydrophilicity based on membrane permeability aligns with the results obtained from comparing D_z values, indicating that the promoted hydrophilicity of membranes will reduce the water flux, which is also found in other NEMD simulation works [34,41,42].

Since the separation of Li^+ and Mg^{2+} is the most concerns in this work, we then focus on the impact of hydrophilicity on the retention rate and selectivity of Mg^{2+}/Li^+ after confirming that hydrophilicity of the TpPa membranes can be adjusted by charge modification. The dependence of ion retention rate and Li^+/Mg^{2+} selectivity on the membrane hydrophilicity is illustrated in Fig. 2d. It can be observed that the retention rate of Li^+ rises promptly from 13.7 % to 72.0 % as hydrophilicity increases from 0.5q to 0.8q. Subsequently, the increase in retention rate of Li^+ slows down as membrane hydrophilicity continues to increase and reaches a maximum of 90.3 %. Meanwhile, the retention rate of Mg^{2+} is lower than 10 % when the membrane hydrophilicity is weaker than 1.2q. The permeation of Mg^{2+} starts to be hindered as the hydrophilicity increases to 1.2q. The retention rate of Mg^{2+} rises to the highest value of 28.4 % with hydrophilicity of 1.4q. It then decreases to 13.3 % when the membrane hydrophilicity reaches maximum (1.6q). Based on the retention rates of these two ions, the Mg^{2+}/Li^+ selectivity ($S_{Mg/Li}$) can be calculated by Eq. (3). The purple circles in Fig. 2d shows that $S_{Mg/Li}$ gradually increases with the membrane hydrophilicity, from 1.2 when 0.5q to 9.0 at 1.6q.

The results of selectivity reveal that the strongly hydrophilic TpPa membrane indeed achieves the goal of selectively permeating Mg^{2+} while retaining Li^+. It can be also observed from the retention data that the enhancement of $S_{Mg/Li}$ is correlated with the continuous increase in retention rate of Li^+. To elucidate the reason why the strongly hydrophilic TpPa membrane impedes the passage of Li^+, we calculate the *xy*-plane density distribution of Li^+ within the membrane and analyze the transport behavior of Li^+ within the membrane. As shown in Fig. 3a, there exists high-density regions of Li^+ near the oxygen atoms on TpPa and it contains an average of three sites, rather than six, in each pore. To further understand the interaction between Li^+ and TpPa pore walls, we analyze the radial distribution functions (RDFs) between Li^+ and oxygen atoms on TpPa of various hydrophilicity (shown in Fig. 3b). For the case of 0.5q, there is almost no peak, suggesting that the mobility of Li^+ within this membrane is rarely affected by the pores, hence the low retention rates for both cations. The first peak of RDF appears at approximately 2 Å as the membrane hydrophilicity increases to 0.8q. The height of the first peak rises with the promoted membrane hydrophilicity, indicating the enhanced forces between Li^+ and TpPa pore walls due to the promoted membrane hydrophilicity. This strong interaction leads to the restricted movement of Li^+ in TpPa pores, and consequently results in a decrease in permeation rate of Li^+ and a rapid increase in retention rate of Li^+. The peak height slightly increases as hydrophilicity further increases and it is consistent with the trend of slower increase in the retention rate of Li^+.

To further elucidate the relationship between the variation in retention rate and the interaction between Li^+ and TpPa, we then pay more attention to the molecular details of ions and water inside membranes. Since retention rate of ions arises from both pore sieving and intra-pore diffusion effects [29], we then distinct the pore sieving effect from the intra-pore diffusion one. According to Eq. (2), the sources of ion retention can be divided into two parts: pore sieving effect (c_{in}/c_0) and intra-pore diffusion effect (v_i/v_w), expressed as follows:

$$R = 1 - \frac{c_{in}}{c_0}\frac{v_i}{v_w} \tag{5}$$

where the first part (c_{in}/c_0) represents the ratio of intra-pore ion concentration to initial ion concentration, indicating the pore sieving effect. The second part (v_i/v_w) represents the flow rate ratio of ion to water molecule within the membranes, indicating the intra-pore diffusion effect. The intra-pore diffusion effect is calculated by determining the residence time of ions and water molecules within the membranes [29]. As discussed above, some cations have strong interaction with TpPa pore walls, resulting in the adsorption of cations onto pore walls. Consequently, the v_i/v_w values are close to zero for some cations in our cases, which is unfavorable for the subsequent analysis. Therefore, we directly record the average distance traveled by ions and water molecules within a unit time (10 ps) based on simulation trajectories and then calculate their flow rates. By this method, we can determine the main factors influencing ion retention by analyzing the magnitudes of c_{in}/c_0 and v_i/v_w.

Fig. 4a shows the results of pore sieving effect for each case. For Mg^{2+} (blue line), the c_{in}/c_0 value is close to 1.0 when the membrane hydrophilicity is weak (0.5q). It indicates that the resistance for Mg^{2+} entering the pores is similar to that of water molecules. The c_{in}/c_0 value for Mg^{2+} remains around 0.6 as membrane hydrophilicity increases. It suggests that Mg^{2+} has higher pore entry resistance compared to water molecules for these cases. The blue line in Fig. 4b represents the flow rate ratio of Mg^{2+} to that of water molecules within membranes (i.e., intra-pore diffusion effect). This ratio does not change significantly with membrane hydrophilicity variations. It is slightly higher than 1.0 for all cases, indicating that the flow rate of Mg^{2+} within the membrane is slightly higher than that of water molecules. This can be attributed to the fact that Mg^{2+} is divalent ion with a well-defined and rigid hydration

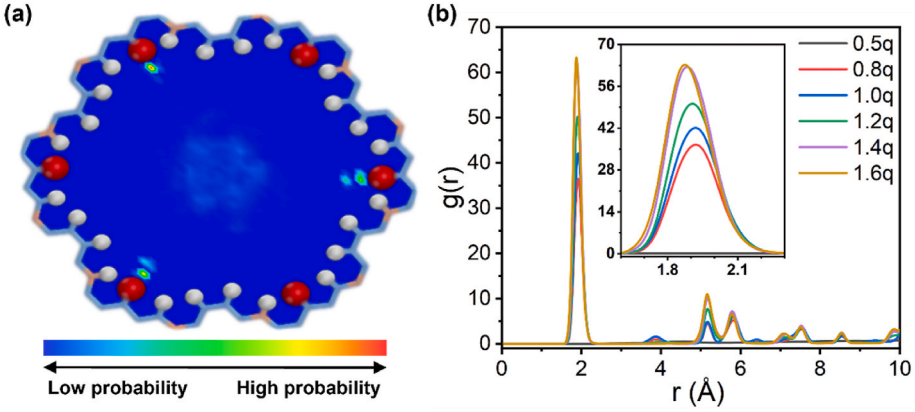

Fig. 3. (a) *xy*-plane density distribution of Li^+ within the membrane in the case of 1.0q. (b) Radial distribution functions (RDFs) between Li^+ and oxygen atoms of TpPa of various hydrophilicity. The inset shows an enlarged display of the region r = 1.6–2.3 Å.

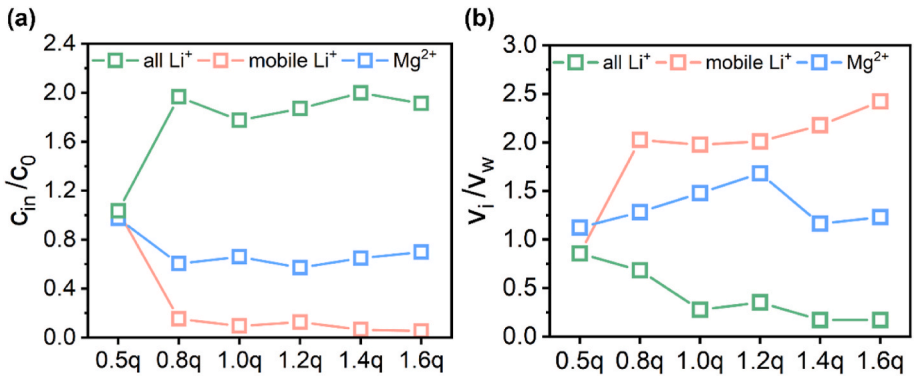

Fig. 4. (a) Pore sieving effect and (b) intra-pore diffusion effect in TpPa membranes of various hydrophilicity. The green squares represent all Li^+, the red squares represent mobile Li^+, and the blue squares represent Mg^{2+} inside the membranes. (For interpretation of the references to colour in this figure legend, the reader is referred to the Web version of this article.)

shell. The microstate of their hydration will not change much from the attraction from atoms of pore walls, thus avoiding a decrease in mobility. In contrast, water molecules can form hydrogen bonds with TpPa pore walls, resulting in attraction that can reduce the flow rate of water molecules within membranes.

The green symbols in Fig. 4a represents the ratio of all Li^+ within the membrane to the initial Li^+ concentration, which approaches 1.0 in TpPa membranes with the weakest hydrophilicity. This ratio rapidly rises to nearly 1.9 as membrane hydrophilicity increases to 0.8q and remains around this value. It indicates the higher concentration of Li^+ within membranes of stronger hydrophilicity compared to the one outside membranes. This finding is consistent with the findings in our previous work, indicating that Li^+ with weaker hydration structures are more likely to enter TpPa membranes [35].

According to Eq. (5), the increase in c_{in}/c_0 leads to the decrease in retention rate. However, in this study, the retention rate of Li^+ increases with the increase in c_{in}/c_0 values. As discussed above, Li^+ has strong interaction with TpPa pore walls, resulting in the adsorption of Li^+ onto pore walls. Consequently, the v_i/v_w values are close to zero for some cases. The green symbols in Fig. 4b represents the flow rate ratio of all Li^+ to water molecules within the membrane. It can be observed that the v_i/v_w values of Li^+ gradually decrease to close to zero as membrane hydrophilicity increases, confirming the state of significant Li^+ adsorption. The adsorbed state does not contribute to the flux of Li^+ in spite of higher Li^+ concentrations within the membrane, so they are unfavorable for the subsequent analysis. Therefore, we c_{in}/c_0 v_i/v_w calculated the flow rate for each Li^+, and plot the distribution of flow rate in Fig. S1. It is found that most flow rate locates at less than 0.03 Å/ps, and there is an obvious gap between lower and higher flow rate. Based on Fig. S1, we prefer to selecting value of 0.03 Å/ps to distinguish adsorbed Li^+ and mobile Li^+, and then exclude adsorbed Li^+ when calculating the pore sieving and intra-pore diffusion effect. The c_{in}/c_0 values of mobile Li^+ shown in Fig. 4a as the red line are much lower compared to c_{in}/c_0 of Mg^{2+}, which is the reason for much higher retention rate of Li^+ than that of Mg^{2+}.

In terms of the flow rate of mobile Li^+ within membranes, it is close to the flow rate of water molecules when the membrane hydrophilicity is weak (0.5q). This indicates that the resistance for Li^+ to pass through the membrane is comparable to that for water molecules as both Li^+ and water molecules have very little interaction with TpPa pore walls. The v_i/v_w values of mobile Li^+ become significantly greater than 1.0 as the membrane hydrophilicity increases to 0.8q and then slightly increase with promoted hydrophilicity. According to Eq. (5), these Li^+, which move faster than water molecules and Mg^{2+}, should lead to a decrease in retention rate of Li^+. However, it is evident from Fig. 2d that the retention rate of Li^+ is significantly higher than that of Mg^{2+}. This indicates that the high retention rate of Li^+ is significantly influenced by the pore sieving effect rather than the intra-pore diffusion effect when the membrane hydrophilicity increases. In other words, the large amount of adsorbed Li^+ inside the membrane prevents the entrance of additional Li^+ into the membrane due to the high concentration of Li^+ already present inside.

Compared to the non-adsorbed case (0.5q), the adsorbed Li^+ within the membrane exhibits a certain enhancement in the mobility of other mobile Li^+ and Mg^{2+}. This may be attributed to the co-ion repulsion effect, known as the Donnan effect. We calculate the radial distribution functions (RDFs) between different ions at weak hydrophilicity (0.5q) and strong hydrophilicity (1.6q). From Fig. 5a, the first peak positions of Li^+ with Li^+ and Mg^{2+} within the membrane are 5.9 Å and 6.8 Å, respectively. However, these two peaks come to 7.1 Å and 7.6 Å at strong hydrophilicity, respectively. The smaller peak positions at weak hydrophilicity indicate closer distances between ions of the same charge and it suggests a weaker repulsion effect between ions with the same charge. On the other side, the larger peak positions suggest a stronger repulsion effect of adsorbed Li^+ against mobile Li^+ and Mg^{2+} at strong hydrophilicity. It counteracts the attraction of the pore walls on mobile Li^+ and Mg^{2+} and thereby enables mobile Li^+ and Mg^{2+} to exhibit higher mobility within the pore compared to water molecules. This increase in the mobility of mobile Li^+ and Mg^{2+} within the membrane due to co-ion repulsion effects can also be attributed to the Donnan effect.

The Donnan effect helps understanding the reason for more quick transport of Mg^{2+}. In order to find out why it is harder for Li^+ to enter Li^+-adsorbed membranes, we calculate the potential of mean force (PMF) for Li^+ and Mg^{2+} when they enter the Li^+-adsorbed membrane (shown in Fig. S4). It is evident that Li^+ has higher energy barrier to enter the membrane than Mg^{2+}. It can be seen from Fig. S5 that more water molecules need to be removed from the hydration layer when Li^+ enter the membrane. Furthermore, we focus on the reason for such high energy barrier for Li^+. The Li^+-adsorbed membrane has positive charge due to the additional charged particle (Li^+) adsorbed in onto pore wall. The extra positive charge of membranes is expected to repel Mg^{2+} due to the nature of divalence for Mg^{2+}. However, when we take close investigations of Mg^{2+} in solution, it is found that, the Mg^{2+} will form ion pair with Cl^- to reduce its valence state (Fig. S6). To confirm this observation, we calculate the RDF of Mg^{2+}-Cl^- and Li^+-Cl^- when all three ions are coexistence in solution of water but without membranes. Although the concentration of Mg^{2+} is as low as 0.141 mol L^{-1}, the first peak in Fig. S8 indicates the ion pair of Mg^{2+}-Cl^-. This result is similar to the condition when ions are in the TpPa membranes (Fig. S7). This ion pair is hard to observe for Li^+-Mg^{2+}. We believe the existence of Mg^{2+}-Cl^- ion pair result in the lower energy barrier for Mg^{2+} to enter the Li^+-adsorbed membrane.

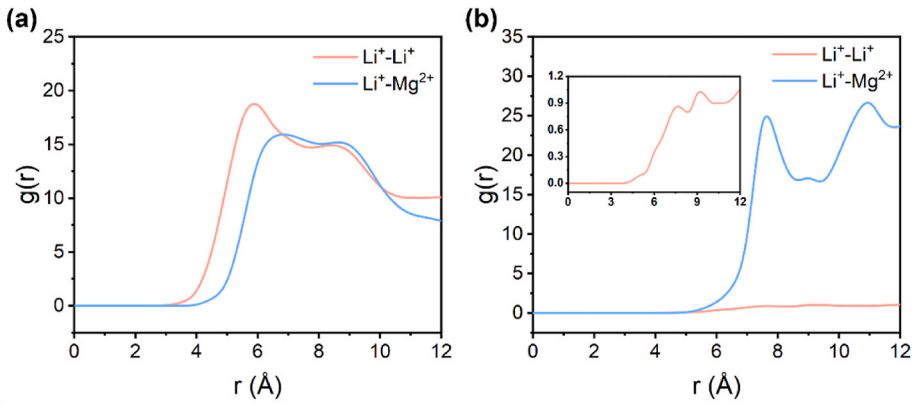

Fig. 5. Radial distribution functions (RDFs) of adsorbed Li^+ with mobile Li^+ and Mg^{2+} at (a) weak hydrophilicity (0.5q) and (b) strong hydrophilicity (1.6q). The inset in (b) shows a magnified view of the RDF between adsorbed Li^+ and mobile Li^+.

3.2. Hydrophilicity adjustment based on chemical groups

In the previous sections, the variations of membrane hydrophilicity by adjusting atomic charges concluded that strong hydrophilicity can reach the goal of Mg^{2+} permeation and Li^+ retention in TpPa membranes. Although this method of adjusting atomic charges can study the influence of membrane hydrophilicity on ion-rejection mechanism by single factor, it is difficult to replicate this process in practical experiments. In practice, common experimental methods for modulating the hydrophilicity and hydrophobicity of COFs membranes involve grafting functional groups onto the pore walls [43,44]. Therefore, we modify the TpPa membrane by grafting different hydrophilic functional groups such as amino, carboxyl, and sulfonic acid groups onto the TpPa pore walls.

Pore size of grafted TpPa is significantly affected due to the differences in molecular size of the grafted functional groups. To understand the changes in pore size, we use Zeo++ software [45] to calculate the minimum pore size of the membranes of various grafting. As shown in Fig. 6a, the minimum pore size of TpPa-NH_2, TpPa-COOH, TpPa-SO_3H are 13.68, 11.57 and 10.84 Å, respectively, which are all significantly larger than the hydrated diameters of Li^+ and Mg^{2+}. However, it should be noticed that there still exist gaps close to the TpPa-R pore walls. It means that relying solely on the minimum pore size to determine the region inside the membrane where ions and water molecules can pass may cause some deviations.

Multiple factors would have impact on comparing the hydrophilicity of TpPa-NH_2, TpPa-COOH, and TpPa-SO_3H. Therefore, we compute the density distribution of water molecules along the *xy*-plane within the membrane and calculate the effective mass transfer area of the membrane pores based on this. As illustrated in Fig. 6b, taking TpPa as an example, all regions where water molecules have appeared are defined as the effective mass transfer area. The calculation results, as shown in Fig. 6c, indicate that the pore area of the three grafted TpPa-R is all around 210 $Å^2$. Comparisons of water flux can be attributed to the influence of membrane hydrophilicity since the effective area for water molecules to pass through is approximately the same.

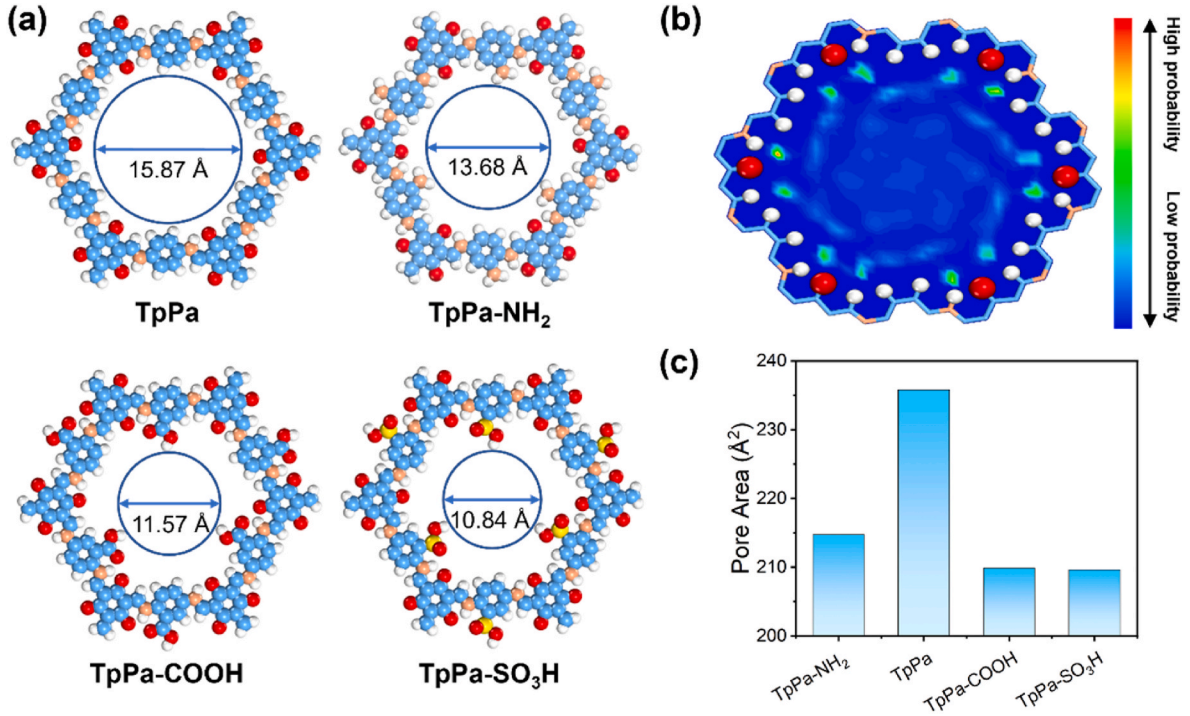

Fig. 6. (a) Models and pore diameter of different modified TpPa-R. (b) *xy*-plane density distribution of oxygen atoms in water molecules within the TpPa membrane. (c) The pore area of each TpPa-R membrane.

Similar to the previous analysis, we compute the mean square displacement of water molecules in the z-direction within the modified TpPa-R membranes, as shown in Fig. 7a. The curves approximately form straight lines. Their slopes represent the self-diffusion coefficients (D_z) of each TpPa-R membrane, respectively. Four TpPa-R membranes are arranged on the x-axis of the graph based on the magnitude of their slopes, as depicted in Fig. 7b. The decreasing values of D_z of four TpPa-R membranes indicate that the membrane hydrophilicity gradually increases. Fig. 7c displays the number of water molecules passing through four TpPa-R membranes in unit time (ns). The water flux of TpPa-NH_2 is much higher than that of TpPa despite its smaller pore area. This indicates that TpPa-NH_2 is more hydrophobic than TpPa without grafting. On the other hand, the effective mass transfer areas of TpPa-COOH and TpPa-SO_3H are similar. However, TpPa-SO_3H is more hydrophilic and this results in a lower water flux compared to TpPa-COOH.

Fig. 7c shows the relationship between the retention rate of Li^+ and Mg^{2+} and $S_{Mg/Li}$ of TpPa and modified TpPa-R. TpPa-NH_2 maintains a high water permeability while exhibiting low retention rate for both cations. It is similar to the results obtained from TpPa in cases of weak hydrophilicity as shown in Fig. 2. TpPa grafted with carboxyl and sulfonic acid exhibit retention rate for Li^+ of approximately 84.3 % and 94.1 %, respectively. TpPa-SO_3H achieves a retention rate for Mg^{2+} of 53.0 %. The results of $S_{Mg/Li}$ are similar to TpPa with different hydrophilicities. TpPa-NH_2 shows low selectivity for both Li^+ and Mg^{2+} when the membrane hydrophilicity is weak. There exists a sharp increase in the retention rate of Li^+ as the membrane hydrophilicity increases. $S_{Mg/Li}$ of TpPa-SO_3H reaches highest of approximately 8.0.

To corroborate the mechanism of TpPa membrane's retention of Li^+ as discussed earlier, we also analyze pore sieving effect and intra-pore diffusion effect of three grafted TpPa-R membranes, as shown in Fig. 8. The c_{in}/c_0 values of ions inside the TpPa-NH_2 membrane are all around 1.0, indicating that the ion concentration inside the membrane is approximately equal to the initial concentration. At the same time, ions move faster than water molecules. This result is similar to the findings shown in Fig. 4 due to the weakest hydrophilicity of TpPa-NH_2 membranes among the four kinds of membranes. The variation trend of c_{in}/c_0 values for TpPa-COOH and TpPa-SO_3H is similar to TpPa with different hydrophilicities. A large number of Li^+ aggregates in the membrane and is adsorbed on the pore walls. This results in few Li^+ passing through the pores. The concentration of Li^+ inside the membrane is higher than that in the bulk phase. This makes it difficult for Li^+ outside the membrane to enter the pores and leads to a higher retention rate of Li^+. In Fig. 8b, the hydrophilicity of three grafted COF membranes gradually increases. It leads to a gradual decrease in the flow rate of Li^+ passing through the membrane and results in a slight increase in the membrane's retention rate of Li^+. It is in accordance with the results observed in Fig. 7d. The decrease in the v_i/v_w of Mg^{2+} in TpPa-SO_3H membranes makes the retention rate of Mg^{2+} grow up to 53.0 %.

4. Conclusions

In this study, we use NEMD simulations to conduct an in-depth investigation into the influence of hydrophilicity on the Li^+ and Mg^{2+} permeation through COF membranes. Firstly, the TpPa is selected because it has enough large pore size for the free penetration of Mg^{2+} and water molecules. The hydrophilicity of TpPa membranes is then tuned by adjusting the partial charge intensity of each atom of TpPa. Such method could exclude other influence but only hydrophilicity. It is found that enhanced hydrophilicity facilitates the achievement of goals for Mg^{2+} exclusion and Li^+ retention. The membrane hydrophilicity gradually increases with increasing charge, significantly enhancing the retention rate of Li^+ while impeding Mg^{2+} to a lesser extent. Further analysis reveals that the interaction force between Li^+ and TpPa pore walls is strengthened in highly hydrophilic membranes. It restricts the entry of Li^+ from outside the membrane and leads to an increase in its retention rate. The adsorption of Li^+ within the membrane enhances the mobility of mobile Li^+ and Mg^{2+} due to the Donnan effect. Meanwhile, we take the method of grafting functional groups to alter the hydrophilicity of TpPa membranes (denoted as TpPa-R), which is corresponding to the modification methods usually used in experiments.

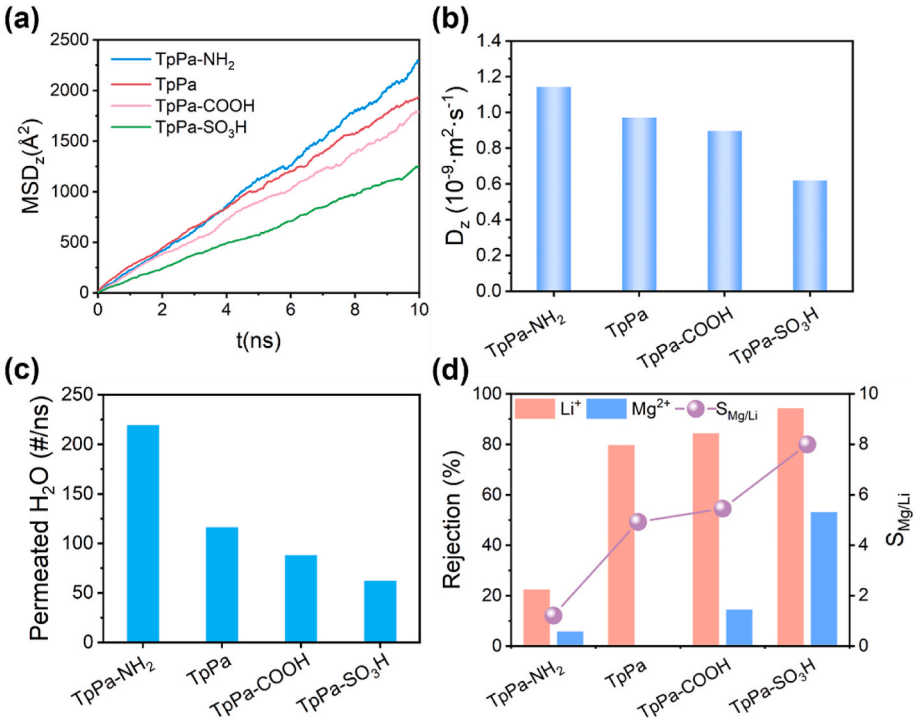

Fig. 7. (a) Mean square displacement and (b) self-diffusion coefficients of water molecules along the z-direction for four TpPa-R membranes at the equilibrium MD simulations of the pure water case. (c) The number of water molecules passing through the membranes per unit time (ns). (d) The relationship between the retention rate of Li^+ and Mg^{2+} and $S_{Mg/Li}$ for the four TpPa-R membranes.

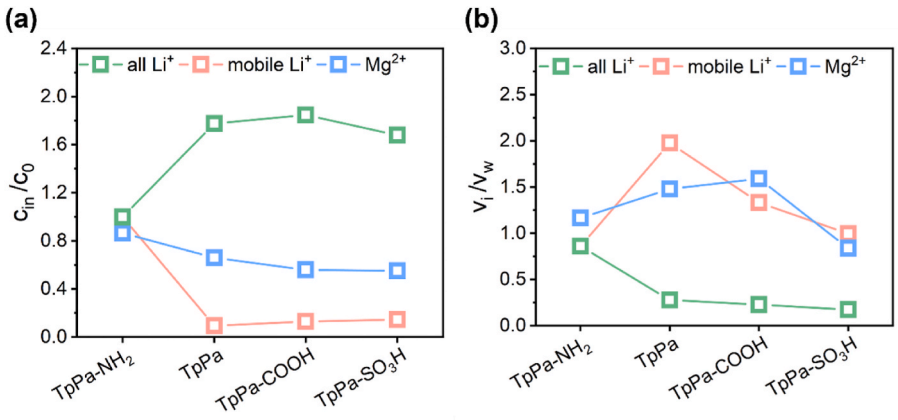

Fig. 8. (a) c_{in}/c_0 and (b) v_i/v_w for the four TpPa-R membranes. The green squares represent all Li^+ inside the membrane, the red squares represent the mobile Li^+, and the blue squares represent Mg^{2+} inside the membranes. (For interpretation of the references to colour in this figure legend, the reader is referred to the Web version of this article.)

Grafting various groups results in changes in pore area, thereby influencing water permeability and ion retention rate. We further elucidate the mechanism of ion permeation for various TpPa-R membranes through analysis of pore sieving effect and intra-pore diffusion effect. The conclusion that the adsorption of Li^+ onto hydrophilic pore walls will lead to higher Mg^{2+}/Li^+ selectivity is also found in these cases. These findings in this work provide an important guidance for designing COF membranes with specific selectivity and permeability.

CRediT authorship contribution statement

Ming Liu: Writing – original draft, Investigation, Data curation. **Mingjie Wei:** Writing – review & editing, Validation, Funding acquisition. **Gan Liu:** Methodology, Investigation. **Daiwen Li:** Investigation. **Zhe Zhang:** Validation, Methodology. **Yong Wang:** Writing – review & editing, Supervision, Funding acquisition, Conceptualization.

Declaration of competing interest

The authors declare that they have no known competing financial interests or personal relationships that could have appeared to influence the work reported in this paper.

Data availability

Data will be made available on request.

Acknowledgement

This work was financially supported by the National Natural Science Foundation of China (21921006, 22278206, 22308147). The authors also thank the High Performance Computing Centre of Nanjing Tech University for supporting the computational resources.

Appendix A. Supplementary data

Supplementary data to this article can be found online at https://doi.org/10.1016/j.memsci.2024.123247.

References

[1] G. Harper, R. Sommerville, E. Kendrick, L. Driscoll, P. Slater, R. Stolkin, A. Walton, P. Christensen, O. Heidrich, S. Lambert, A. Abbott, K. Ryder, L. Gaines, P. Anderson, Recycling lithium-ion batteries from electric vehicles, Nature 575 (2019) 75–86, https://doi.org/10.1038/s41586-019-1682-5.
[2] S. Yang, F. Zhang, H. Ding, P. He, H. Zhou, Lithium metal extraction from seawater, Joule 2 (2018) 1648–1651, https://doi.org/10.1016/j.joule.2018.07.006.
[3] Y. Qiu, H. Ruan, C. Tang, L. Yao, J. Shen, A. Sotto, Study on recovering high-concentration lithium salt from lithium-containing wastewater using a hybrid reverse osmosis (RO)–Electrodialysis (ED) process, ACS Sustainable Chem. Eng. 7 (2019) 13481–13490, https://doi.org/10.1021/acssuschemeng.9b03108.
[4] P. Greim, A.A. Solomon, C. Breyer, Assessment of lithium criticality in the global energy transition and addressing policy gaps in transportation, Nat. Commun. 11 (2020) 4570, https://doi.org/10.1038/s41467-020-18402-y.
[5] L. Guo, Z. Guo, J. Wang, P. Zhang, Z. Huang, Z. Ji, Flexible lithium selective composite membrane for direct lithium extraction from high Na/Li ratio brine, J. Membr. Sci. 703 (2024) 122843–122852, https://doi.org/10.1016/j.memsci.2024.122843.
[6] M. Ahmed, W.H. Shayya, D. Hoey, A. Mahendran, R. Morris, J. Al-Handaly, Use of evaporation ponds for brine disposal in desalination plants, Desalination 130 (2000) 155–168, https://doi.org/10.1016/S0011-9164(00)00083-7.
[7] H. Yu, J. Zhang, J. Bao, X. Jiang, R. Yang, G. Zhou, S. Yin, X. Zhang, G. He, N. Zhang, Preferential permeation of Li+ over Mg2+ through homogenously negatively-charged nanochannels, Desalination 582 (2024) 117653–117659, https://doi.org/10.1016/j.desal.2024.117653.
[8] H. Vikström, S. Davidsson, M. Höök, Lithium availability and future production outlooks, Appl. Energy 110 (2013) 252–266, https://doi.org/10.1016/j.apenergy.2013.04.005.
[9] J. Xu, Y. Jin, K. Liu, N. Lyu, Z. Zhang, B. Sun, Q. Jin, H. Lu, H. Tian, X. Guo, D. Shanmukaraj, H. Wu, M. Li, M. Armand, G. Wang, A green and sustainable strategy toward lithium resources recycling from spent batteries, Sci. Adv. 8 (2022) eabq7948, https://doi.org/10.1126/sciadv.abq7948.
[10] S. Xu, J. Song, Q. Bi, Q. Chen, W.-M. Zhang, Z. Qian, L. Zhang, S. Xu, N. Tang, T. He, Extraction of lithium from Chinese salt-lake brines by membranes: design and practice, J. Membr. Sci. 635 (2021) 119441–119462, https://doi.org/10.1016/j.memsci.2021.119441.
[11] Q. Li, H. Liu, Y. Ji, Z. Cui, F. Yan, M. Younas, J. Li, B. He, Efficiently rejecting and concentrating Li+ by nanofiltration membrane under a reversed electric field, Desalination 535 (2022) 115825–115835, https://doi.org/10.1016/j.desal.2022.115825.
[12] J. Hou, H. Zhang, A.W. Thornton, A.J. Hill, H. Wang, K. Konstas, Lithium extraction by emerging metal–organic framework-based membranes, Adv. Funct. Mater. 31 (2021) 2105991, https://doi.org/10.1002/adfm.202105991.
[13] D. Lu, T. Ma, S.S. Lin, Z.J. Zhou, G. Li, Q.F. An, Z.K. Yao, Q. Sun, Z.L. Sun, L. Zhang, Constructing a selective blocked-nanolayer on nanofiltration membrane via surface-charge inversion for promoting Li+ plus permselectivity over Mg2+, J. Membr. Sci. 635 (2021) 119504–119513, https://doi.org/10.1016/j.memsci.2021.119504.
[14] Z. Si, Z. Zhang, C. Yin, T. Ju, M. Wei, J. Huang, Y. Wang, Engineering transport highways in microporous membranes for lithium extraction: the double role of covalent organic frameworks, J. Membr. Sci. 680 (2023) 121759–121767, https://doi.org/10.1016/j.memsci.2023.121759.
[15] F.G. Donnan, Theory of membrane equilibria and membrane potentials in the presence of non-dialysing electrolytes. A contribution to physical-chemical physiology, J. Membr. Sci. 100 (1995) 45–55, https://doi.org/10.1016/0376-7388(94)00297-C.
[16] C.S. Diercks, O.M. Yaghi, The atom, the molecule, and the covalent organic framework, Science 355 (2017) 923–931, https://doi.org/10.1126/science.aal1585.
[17] P. Li, B. He, X. Li, Y. Lin, S. Tang, Chitosan-linked dual-sulfonate COF nanosheet proton exchange membrane with high robustness and conductivity, Small 19 (2023) 2302060–2302070, https://doi.org/10.1002/smll.202302060.
[18] S. Yuan, X. Li, J. Zhu, G. Zhang, P. Van Puyvelde, B. Van der Bruggen, Covalent organic frameworks for membrane separation, Chem. Soc. Rev. 48 (2019) 2665–2681, https://doi.org/10.1039/c8cs00919h.

[19] M.S. Lohse, T. Bein, Covalent organic frameworks: structures, synthesis, and applications, Adv. Funct. Mater. 28 (2018) 1705553, https://doi.org/10.1002/adfm.201705553.
[20] T. Zhu, Y. Kong, B. Lyu, L. Cao, B. Shi, X. Wang, X. Pang, C. Fan, C. Yang, H. Wu, Z. Jiang, 3D covalent organic framework membrane with fast and selective ion transport, Nat. Commun. 14 (2023) 5926, https://doi.org/10.1038/s41467-023-41555-5.
[21] H. Wang, Y. Zhai, Y. Li, Y. Cao, B. Shi, R. Li, Z. Zhu, H. Jiang, Z. Guo, M. Wang, L. Chen, Y. Liu, K.-G. Zhou, F. Pan, Z. Jiang, Covalent organic framework membranes for efficient separation of monovalent cations, Nat. Commun. 13 (2022) 7123, https://doi.org/10.1038/s41467-022-34849-7.
[22] Q. Wang, J. Song, X. Gao, L. Liu, C. Liu, Carbon nanotube membranes for the separation of Li+ and Mg2+ ions: effect of functional groups with charges, Desalination 540 (2022) 115996–116004, https://doi.org/10.1016/j.desal.2022.115996.
[23] Y. Zhang, T. Fang, Q. Hou, Z. Li, Y. Yan, Water desalination of a new three-dimensional covalent organic framework: a molecular dynamics simulation study, Phys. Chem. Chem. Phys. 22 (2020) 16978–16984, https://doi.org/10.1039/d0cp01792b.
[24] M. Tong, Y. Lan, Q. Yang, C. Zhong, Exploring the structure-property relationships of covalent organic frameworks for noble gas separations, Chem. Eng. Sci. 168 (2017) 456–464, https://doi.org/10.1016/j.ces.2017.05.004.
[25] T. Lu, F. Chen, Multiwfn: a multifunctional wavefunction analyzer, J. Comput. Chem. 33 (2011) 580–592, https://doi.org/10.1002/jcc.22885.
[26] S.J. Plimpton, Fast Parallel algorithms for short-range molecular dynamics, J. Comput. Phys. 117 (1995) 1–19, https://doi.org/10.1006/jcph.1995.1039.
[27] F. Xu, L. Dai, Y. Wu, Z. Xu, Li+/Mg2+ separation by membrane separation: the role of the compensatory effect, J. Membr. Sci. 636 (2021) 119542–119550, https://doi.org/10.1016/j.memsci.2021.119542.
[28] F. Xu, Y. Wang, C. Lian, Z. Xu, Fast proton-selective transport through covalent organic frameworks in aqueous phase, J. Membr. Sci. 648 (2022) 120361–120370, https://doi.org/10.1016/j.memsci.2022.120361.
[29] F. Xu, M. Wei, X. Zhang, Y. Wang, Ion rejection in covalent organic frameworks: revealing the overlooked effect of in-pore transport, ACS Appl. Mater. Interfaces 11 (2019) 45246–45255, https://doi.org/10.1021/acsami.9b18234.
[30] B. Lyu, M. Wang, J. Jiang, Z. Jiang, Molecular design of covalent−organic framework membranes for Li+/Mg2+ separation: significant charge effect, J. Membr. Sci. 662 (2022) 120976–120983, https://doi.org/10.1016/j.memsci.2022.120976.
[31] H.J.C. Berendsen, J.R. Grigera, T.P. Straatsma, The missing term in effective pair potentials, J. Phys. Chem. 91 (1987) 6269–6271, https://doi.org/10.1021/j100308a038.
[32] I.S. Joung, T.E. Cheatham III, Determination of Alkali and Halide Monovalent Ion Parameters for Use in Explicitly Solvated Biomolecular Simulations, J. Phys. Chem. B 112 (2008) 9020–9041. https://doi.org/10.1021/jp8001614.
[33] P. Li, B.P. Roberts, D.K. Chakravorty, K.M. Merz, Rational design of particle mesh ewald compatible Lennard-Jones parameters for +2 metal cations in explicit solvent, J. Chem. Theory Comput. 9 (2013) 2733–2748, https://doi.org/10.1021/ct400146w.
[34] F. Xu, M. Wei, X. Zhang, Y. Wang, Effect of hydrophilicity on water transport through sub-nanometer pores, J. Membr. Sci. 611 (2020) 118297–118304, https://doi.org/10.1016/j.memsci.2020.118297.
[35] D. Liao, Z. Xu, M. Wei, Y. Wang, Interference mechanism of cations on transport of lithium and magnesium inside COF nanofiltration membranes, Mol. Simul. 48 (2022) 1369–1377, https://doi.org/10.1080/08927022.2022.2094372.
[36] M. Guan, Q. Liu, H. Zhang, Q. Li, J. Xu, M. Cai, W. Lin, W. Li, D. Yang, Effects of linking group on the desalination performance of three-dimensional covalent organic framework membranes, Desalination 559 (2023), https://doi.org/10.1016/j.desal.2023.116644.
[37] F. Xu, M. Wei, Y. Wang, Effect of hydrophilicity on ion rejection of sub-nanometer pores, Sep. Purif. Technol. 257 (2021) 117937–117944, https://doi.org/10.1016/j.seppur.2020.117937.
[38] W. Humphrey, A. Dalke, K. Schulten, VMD: visual molecular dynamics, J. Mol. Graph. 14 (1996) 33–38, https://doi.org/10.1016/0263-7855(96)00018-5.
[39] F. Xu, Y. Song, M. Wei, Y. Wang, Water flow through interlayer channels of two-dimensional materials with various hydrophilicities, J. Phys. Chem. C 122 (2018) 15772–15779, https://doi.org/10.1021/acs.jpcc.8b04719.
[40] C. Wang, B. Wen, Y. Tu, R. Wan, H. Fang, Friction reduction at a superhydrophilic surface: role of ordered water, J. Phys. Chem. C 119 (2015) 11679–11684, https://doi.org/10.1021/acs.jpcc.5b02024.
[41] F. Xu, M. Wei, X. Zhang, Y. Song, W. Zhou, Y. Wang, How pore hydrophilicity influences water permeability? Research (2019) 1–10, https://doi.org/10.1155/2019/2581241, 2019.
[42] J. Goldsmith, C.C. Martens, Molecular dynamics simulation of salt rejection in model surface-modified nanopores, J. Phys. Chem. Lett. 1 (2010) 528–535, https://doi.org/10.1021/jz900173w.
[43] X. Shi, Z. Zhang, S. Fang, J. Wang, Y. Zhang, Y. Wang, Flexible and robust three-dimensional covalent organic framework membranes for precise separations under extreme conditions, Nano Lett. 21 (2021) 8355–8362, https://doi.org/10.1021/acs.nanolett.1c02919.
[44] Z. Teng, Z. Zhang, H. Yang, Q. Zhang, T. Ohno, C. Su, Atomically isolated Sb(CN)3 on sp2-c-COFs with balanced hydrophilic and oleophilic sites for photocatalytic C-H activation, Sci. Adv. 10 (2024), https://doi.org/10.1126/sciadv.adl5432 eadl5432.
[45] T.F. Willems, C.H. Rycroft, M. Kazi, J.C. Meza, M. Haranczyk, Algorithms and tools for high-throughput geometry-based analysis of crystalline porous materials, Microporous Mesoporous Mater. 149 (2012) 134–141, https://doi.org/10.1016/j.micromeso.2011.08.020.